

Key Points:

- Experiments with Phobos analogs were carried out to evaluate the sputtering by O^+ , C^+ , O_2^+ , and CO_2^+ ions from the Martian atmosphere
- The sputter yield from O ions is lower than previously assumed, and no yield increases due to molecular effects were observed
- Previous predictions that planetary O ions will dominate sputtering in the Martian tail region are supported by the measurements presented

Correspondence to:

P. S. Szabo and F. Aumayr,
szabo@iap.tuwien.ac.at;
aumayr@iap.tuwien.ac.at


Citation:

Szabo, P. S., Biber, H., Jäggi, N., Wappl, M., Stadlmayr, R., & Primetzhofer, D., et al. (2020). Experimental insights into space weathering of phobos: laboratory investigation of sputtering by atomic and molecular planetary ions. *Journal of Geophysical Research: Planets*, 125, e2020JE006583. <https://doi.org/10.1029/2020JE006583>

Received 17 JUN 2020

Accepted 28 OCT 2020

Experimental Insights Into Space Weathering of Phobos: Laboratory Investigation of Sputtering by Atomic and Molecular Planetary Ions

P. S. Szabo¹ , H. Biber¹ , N. Jäggi² , M. Wappl¹ , R. Stadlmayr¹ , D. Primetzhofer³ , A. Nennung⁴ , A. Mutzke⁵ , J. Fleig⁴ , K. Mezger⁶ , H. Lammer⁷ , A. Galli² , P. Wurz² , and F. Aumayr¹ 

¹Institute of Applied Physics, TU Wien, Vienna, Austria, ²Physics Institute, University of Bern, Bern, Switzerland, ³Department of Physics and Astronomy, Uppsala University, Uppsala, Sweden, ⁴Institute of Chemical Technologies and Analytics, TU Wien, Vienna, Austria, ⁵Max-Planck-Institute for Plasma Physics, Greifswald, Germany, ⁶Institute of Geological Sciences, University of Bern, Bern, Switzerland, ⁷Space Research Institute (IWF), Austrian Academy of Sciences, Graz, Austria

Abstract Investigating the space weathering of the Martian moon Phobos represents an important step toward understanding the development from its origin to its present-day appearance. Depending on Phobos' orbital position, its surface is continuously sputtered by the solar wind and planetary ions that originate in the Martian atmosphere. Based on Mars Atmosphere and Volatile Evolution measurements, it has been proposed that sputtering by planetary O^+ and O_2^+ ions dominates in the Martian tail region, where the planet mostly shadows Phobos from the solar wind. In these models, uncertainties for sputtering yield inputs still exist due to the lack of sufficient analog experiments. Therefore, sputtering measurements with O^+ , O_2^+ , C^+ , and CO_2^+ ions between 1 and 5 keV were performed using augite samples as Phobos analogs. The experimental results for O^+ irradiations show smaller mass changes than predicted by SDTrimSP simulations, which probably can be attributed to O implantation enabled by the Fe content of the target. Sputtering with O_2^+ and CO_2^+ in the low keV range shows no deviations in the sputtering yields attributable to molecular effects. Therefore, CO_2^+ ions will most likely be negligible for the sputtering of Phobos according to the current understanding of ion fluxes on the Martian moon. Ultimately, our experiments suggest that the sputtering contribution on Phobos by O ions is about 50% smaller than previously assumed. This does not change the qualitative outcome from previous modeling stating that planetary O ions are by far the dominant sputtering contribution on Phobos in the Martian tail region.

Plain Language Summary The surface of the Martian moon Phobos is continuously eroded by positively charged ions in a process called sputtering, which has changed the moon's surface over the past billions of years. Previous calculations suggest that this sputtering is caused by ions from the solar wind as well as oxygen ions that reach Phobos from the atmosphere of Mars. However, there exists a significant lack of data on how much sputtering each ion causes. This study presents laboratory experiments where the erosion of Phobos analog samples is investigated under irradiation with O^+ , O_2^+ , C^+ , and CO_2^+ ions. The focus was put on oxygen ions and molecular ions that can be expected to escape the Martian atmosphere and cause sputtering of the surface of Phobos. In general, erosion rates are found to be smaller than previously calculated. Additionally, no significant differences in sputtering effects are observed for atomic versus molecular ions. The presented experimental studies support previous conclusions about the unique sputtering conditions on Phobos: in the Martian tail regions, where the planet shadows the solar wind, oxygen ions from the atmosphere of Mars dominate the erosion of the surface of Phobos.

1. Introduction

In recent years, several research efforts have focused on the Mars moon Phobos to investigate its unique space weathering environment (Cipriani et al., 2011). While micrometeoroid impacts are assumed to be negligible for the modification of its surface, Phobos is subject to sputtering by both the solar wind and planetary ions that originate in the Martian atmosphere (Poppe & Curry, 2014). The latter contribution results

© 2020 The Authors.

This is an open access article under the terms of the Creative Commons Attribution License, which permits use, distribution and reproduction in any medium, provided the original work is properly cited.

mostly from the interaction of the solar wind with the planet's atmosphere (Ramstad et al., 2017) and the short distance of Phobos to Mars' surface, which is approximately 6,000 km in an almost circular orbit. In the Martian magnetosphere, atmospheric molecules are ionized, and subsequently, the ions are accelerated in the electromagnetic fields created by the solar wind (Barabash et al., 2007; Dubinin et al., 1993, 2006). Surface erosion on Phobos over billions of years is thus not only connected to solar activity, but also to the Martian atmosphere. Therefore, understanding the space weathering on Phobos is key to determine the still unclear origins of the Martian moons.

So far, observations of the Martian moons have been restricted to remote sensing. For example, near-infrared spectrophotometry has uncovered “redder” and “bluer” regions (Rivkin et al., 2002). Simulations of grain motions due to the orbital eccentricity of Phobos show that blue regions are more likely to feature new material on the surface (Ballouz et al., 2019). Reddening of optical spectra as a result of space weathering is a common finding in general (Marchi et al., 2005). This supports the assumption that space weathering is significantly changing the surface of Phobos.

Sputtering of Phobos has also been investigated as a particle source to form a neutral torus around Mars (Poppe et al., 2016). With a mean radius of 11 km, Phobos has a negligible gravitational pull and the resulting escape velocity is only 11.39 m/s (corresponding to about 7×10^{-7} eV/amu). Thus, not even a tenuous exosphere can be maintained around this small moon. This situation differs from other bodies in the solar system, where exospheres have been a significant topic of research, including Mercury (Leblanc & Johnson, 2010; Pflieger et al., 2015; Wurz & Lammer, 2003), the Moon (Hurley et al., 2017; Wurz et al., 2007), or the Jovian moon Europa (Plainaki et al., 2012; Vorburget & Wurz, 2018). Instead, particles released from the surface of Phobos enter the Martian gravitational field. To better understand and simulate this phenomenon, exact knowledge about the release of particles by sputtering from the surface of Phobos is necessary.

Ion escape from the Martian atmosphere has previously been investigated with the Phobos-2 and Mars Express missions (Verigin et al., 1991). Recently, the Mars Atmosphere and Volatile Evolution (MAVEN) mission has provided a more detailed look into Mars' ion environment (Jakosky et al., 2015; Ramstad et al., 2018). Based on these observations, Nenon et al. (2019) modeled the effect of different sputtering sources on Phobos. Using measurements from the MAVEN instruments Supra thermal And Thermal Ion Composition and Solar Wind Ion Analyzer, the fluxes and energies of different ion species reaching the surface of Phobos were assessed. Over a larger part of Phobos' orbit around Mars, the surface of Phobos is mainly irradiated by the solar wind, which mostly consists of H^+ and He^{2+} ions at energies corresponding to 1 keV/amu (Russell et al., 2016). However, the solar wind is shadowed in Mars' tail, and here the sputtering by atmospheric O^+ and O_2^+ ions with energies between several 100 and several 1,000 eV was calculated to be the dominant process (Nenon et al., 2019). Oxygen ions are the primary contribution to atmospheric ion precipitation on Phobos as O_2 is the most abundant component of upper atmosphere layers (Carlsson et al., 2006; Deighan et al., 2015; Mahaffy et al., 2015). As a consequence, sputtering by CO_2^+ ions is assumed to be negligible (Nenon et al., 2019), even though CO_2 makes up 95% of the Martian bulk atmosphere (Mahaffy et al., 2013).

As an approximated input for their model, Nenon et al. (2019) applied sputtering yields for O ions on monoatomic Ni samples to estimate the total flux of sputtered atoms. They state that experimental investigations on sputtering of planetary analogs are still “limited”. Existing data on sputtering of planetary analog samples give “an uncertainty of roughly a factor of 2” in comparison to their used input values. However, the few existing experiments with analog samples focused on H^+ sputtering or the contribution by multiply charged solar wind ions (see e.g., Barghouty et al., 2011; Hijazi et al., 2017; Szabo et al., 2020a). Here additional potential sputtering effects will occur (Aumayr & Winter 2004). These effects will not play a role for Martian atmospheric ions, where only singly charged ions have been reported (Carlsson et al., 2006).

Additionally, sputtering yields will depend on the sample's chemical composition (Sigmund, 1969) and no clear consensus exists if further effects, such as chemical sputtering, are to be expected when Martian planetary ions interact with the surface of Phobos. Due to missing experimental investigations, it is also still unclear whether molecular effects influence the sputtering by O_2^+ and CO_2^+ ions. Such possible deviations in sputtering behavior would affect how O_2^+ ions have to be considered and if CO_2^+ ions can be neglected for space weathering on Phobos.

These open questions call for laboratory experiments irradiating Phobos analog samples to obtain quantitative data for the sputtering of its surface. We performed sputtering experiments with O^+ , O_2^+ , C^+ , and CO_2^+ using thin augite films deposited on a quartz crystal microbalance (QCM). The elemental composition of these films deposited from pyroxene mineral is similar to current estimations for the surface composition of Phobos (see Section 2.2, Cipriani et al., 2011). Pyroxenes are probably not abundant on the surface of Phobos as no pyroxene absorption lines have been found in infrared investigations of its surface (Fraeman et al., 2014), but a similar elemental composition will still give good insights into sputtering yields. In any case, amorphization of the sample within the ion penetration depth can be expected as a result of space weathering (Carrez et al., 2002).

Ion energies between 1 and 5 keV were used for irradiation to reflect a significant part of the energy spectrum of the ions that reach Phobos. This energy range corresponds to about 50% of the calculated total sputtered flux on Phobos due to O irradiation (Nenon et al., 2019). Comparison with established sputtering simulations using SDTrimSP and Stopping and Range of Ions in Matter (SRIM) will allow extrapolating our conclusions to the remaining relevant energies (Mutzke et al., 2019; Ziegler et al., 2010). These experimental results will thus allow a more accurate modeling of the space weathering effects that occur on Phobos in the Martian tail region.

2. Methods

2.1. Experimental Setup

The sputtering experiments were performed at the electron cyclotron resonance (ECR) ion source setup at TU Wien (Galutschek et al., 2007), which was described in previous publications (see e.g., Szabo et al., 2018).

In this setup, gas is ionized by microwave-driven electron ionization. After extracting the ions from the ECR source and focusing the beam with a quadrupole magnet, the mass-over-charge state ratio m/q is selected with a sector magnetic field. This allows separating specific ions at the desired charge state and ensures a clean ion beam. In the target chamber, the ion beam is scanned uniformly across the sample using a set of electrostatic deflection plates. Samples are mounted on a rotating sample holder that includes a Faraday cup for measurements of the beam current density. Ion beam profiles were obtained before and after each irradiation, while the current was monitored additionally at an aperture in the ion beam optics to check its stability. All experiments were performed at room temperature under ultrahigh vacuum conditions, with base pressures on the order of 10^{-10} mbar.

2.2. Quartz Crystal Microbalance Samples

Thin films of augite $(Ca, Mg, Fe)_2Si_2O_6$ were deposited on QCMs by pulsed laser deposition (PLD). The QCM technique allows in situ, real-time measurements of mass changes of a thin film as a result of, for example, ion irradiation (Hayderer et al., 1999). Here the thickness oscillation of the quartz is driven electronically and the resonance frequency of this oscillation is measured. Its relative change is proportional to the relative mass change of the sample (Sauerbrey, 1959). When the thin film of sample material on the top of the quartz is sputtered, the rate of the frequency change is thus related to the sputtered flux. Total sputtering yields expressed as amu/ion can be calculated when the ion beam current density is considered (Hayderer et al., 1999).

QCM sputtering measurements have been performed by multiple research groups for the investigation of a wide range of space weathering effects, for example, Galli et al. (2017, 2018a, 2018b) investigated the sputtering of ice films under irradiation of different ion species as well as electrons. Potential sputtering yields by multiply charged He and Ar ions were obtained with thin films of anorthite (Hijazi et al., 2014, 2017) and wollastonite $(CaSiO_3)$ (Szabo et al., 2018, 2020a). Additionally, Biber et al. (2020) analyzed the implantation behavior of solar wind He in pyroxene samples from the same deposition batch as the samples used in the present study. For the investigation of bulk samples such as mineral pellets, a QCM can also be used in a catcher configuration, where it is placed next to the irradiated sample. Then the mass increase by sputtered atoms sticking to the catcher QCM can be measured (Berger et al., 2017). Such a setup can also give insights into the angular distribution of sputtered particles (see Li et al. [2017] for measurements with

Table 1
Comparison of the Composition of the Thin Film Samples Used in This Study and Current Estimations About the Surface of Phobos

	Ca	Mg	Fe	Si	O	H	C	Al	Na
Augite ^a	1.8 ± 0.1	8.9 ± 0.3	6.0 ± 0.2	20.5 ± 0.5	60.3 ± 0.9	1.4 ± 0.1	1.1 ± 0.1	-	-
Phobos ^b	0.1	14	9	11	64	-	-	1.5	0.5
Wollastonite ^c	18.4	-	-	19.2	59.4	2.0	1.0	-	-

Note. All values represent concentrations in atomic percent.

Abbreviation: ToF-ERDA, time-of-flight elastic recoil detection analysis.

^aResults from ToF-ERDA analysis (Biber et al. 2020). ^bPoppe and Curry (2014). ^cResults from ToF-ERDA analysis (Szabo et al. 2020a).

structured molybdenum surfaces, and Stadlmayr et al. [2020] for experiments with highly porous tungsten fuzz structures).

Analysis of the original material shows the existence of several phases with varying Ca concentration. However, we focus on characterizing the deposited films on the QCM samples. For the augite samples used in the present study, the same sample preparation and analysis procedures were applied as described by Biber et al. (2020). PLD was performed with a 248 nm KrF excimer laser at 5 Hz and $1 \text{ J}^{-1} \text{ cm}^{-2} \text{ pulse}^{-1}$ for 60 min with a sample temperature of about 300°C. Under the polarization microscope, the augite films were found to be amorphous. This is expected due to the low deposition temperature. Amorphous layers were also observed previously in x-ray diffraction analysis of films deposited from wollastonite with PLD (Szabo et al., 2018). However, sputtering of amorphous and polycrystalline samples behaves similarly and thus the measured sputtering yields are expected to be representative of the sputtering yields for mineral targets (Sigmund, 1969). During prolonged ion bombardment, amorphization of the near-surface region will be anyway expected in a space weathering environment (Carrez et al., 2002).

The thickness and composition of the films were analyzed at Uppsala University with Rutherford backscattering spectrometry (RBS) with 2 MeV He⁺ and time-of-flight elastic recoil detection analysis (ToF-ERDA) with 36 MeV I⁸⁺ (Moro et al., 2019). Film thicknesses of about 150 nm as well as sample compositions close to the stoichiometric pyroxene composition were found. While the Ca, Mg, and Fe concentrations are not fixed by the augite denomination, the pyroxene-characteristic 20% Si and 60% O content of the nominal mineral composition are very well represented in the deposited films. Table 1 gives an overview of the observed atomic concentrations of the analyzed sample from ToF-ERDA as presented in Biber et al. (2020), including H and C contaminations. The values are averaged over the whole film, but very uniform film compositions were measured with ToF-ERDA.

Table 1 also shows a comparison to the Phobos surface composition used in the modeling by Poppe and Curry (2014) and Poppe et al. (2016), originally proposed by Vernazza et al. (2010) and Cipriani et al. (2011). It was derived from asteroid compositions, whose infrared spectra were found to agree well with Phobos. Therefore, still significant uncertainties exist about the actual composition of Phobos. The current consensus on the surface composition of Phobos is, however, well reflected in the element abundances of the used augite sample. General experimental observations with augite samples should thus be representative for the space weathering of Phobos. This is underlined by similar results for SDTrimSP simulations with both compositions (see Section 2.3).

Section 3.2 includes comparison measurements with samples deposited from wollastonite (CaSiO₃). Samples from the same deposition batches were analyzed with RBS and ToF-ERDA in previous sputtering experiments (Szabo et al., 2020a). The composition of the films was found to be very close to stoichiometric (see Table 1).

2.3. Sputtering Simulation Codes

To compare the experimental results with established simulation codes, sputtering calculations were performed with SRIM-2013 and SDTrimSP 6.01 (Mutzke et al., 2019; Ziegler et al., 2010). Both codes are based

Table 2
Comparison of SDTrimSP Simulation Results (Static Mode) of the Sputtering Yields for the Augite Composition and the Assumed Phobos Composition

	Sputtering yield (augite composition) (atoms/ion)	Sputtering yield (Phobos composition) (atoms/ion)	Difference of the Phobos composition
1 keV H	0.013	0.015	+15%
4 keV He	0.087	0.092	+6%
2 keV O	0.711	0.761	+7%
16 keV O	0.605	0.642	+6%

on simulating the collision cascade during ion-solid interaction with the binary collision approximation. In planetary science, SRIM results are often used as the reference for sputtering input. However, discrepancies between SRIM's results and experimental findings have been found in previous work (Hofsäss et al., 2014; Schaible et al., 2017; Szabo et al., 2018, 2020a). In nuclear fusion research, SDTrimSP is more commonly used as it also allows performing dynamic simulations. Simulations in the static mode give the same functionality as SRIM simulations, where sputtering yields are calculated, but changes to the target are not included. In the dynamic mode, however, it is possible to calculate how the composition changes due to preferential sputtering. Ion implantation can either be completely disregarded (corresponding to an immediate outgassing of projectile ions), allowed up to a user-defined maximum concentration or simulated more realistically with several diffusion effects. Finding suitable

values for input parameters such as surface binding energies and diffusion coefficients requires, however, careful comparison with experimental data (Schmitz et al., 2019).

In our previous studies, we have adapted the surface binding energies in SDTrimSP to consistently reproduce wollastonite sputtering yields under He⁺ and Ar⁺ bombardment based on simulations in the static mode (Szabo et al., 2020a). Biber et al. (2020) applied the same set of parameters for the augite films and also found precise agreement with measured He⁺ and Ar⁺ sputtering yields. SDTrimSP simulations presented in this article are therefore also performed with the parameters derived by Szabo et al. (2020a). For the augite samples, the ToF-ERDA analysis results were used as the input for the sample composition.

When SDTrimSP simulations that were performed in the static mode for augite and the assumed Phobos composition (see Section 2.2) are compared, similar results can be found. Total sputtering yields are slightly higher for the assumed Phobos composition, which was tested for normal incidence irradiations with 1 keV H ions, 4 keV He ions, 2 keV O ions, and 16 keV O ions (see Table 2). The observed small differences in the simulated sputtering yields further indicate that the augite samples give representative results for sputtering of the surface of Phobos. Such a behavior is expected as the composition differences are small. The observed variations are mostly caused by the Phobos composition being richer in Mg and poorer in Si. SDTrimSP uses a lower surface binding energy for Mg (1.51 eV for Mg and 4.72 eV for Si), and mass transfer to the somewhat lighter Mg atoms is more effective for light projectile ions such as H, He, and O. Both of these aspects favor the sputtering of a material with more Mg and less Si, which explains the differences between augite and the assumed Phobos composition in the simulation.

3. Results

3.1. O⁺ Measurements on Augite

Augite samples that were freshly inserted into the vacuum chamber were first irradiated with 2 keV Ar⁺ at fluences of several 10¹⁹ ions/m² to clean the sample from surface contamination. Following irradiations with O⁺ ions showed a significant fluence dependence of the sputtering yield. Figure 1a presents an example measurement with 2 keV O⁺ under normal incidence. The experiments give sputtering yields in amu/ion. Sputter yields in atoms/ion are calculated by dividing by the average atomic mass from the ToF-ERDA composition (21.77 amu). The measured sputtering yield starts close to the SDTrimSP prediction (static simulation, dashed line), but then decreases significantly before increasing again and reaching a stable value at a fluence of several 10²⁰ ions/m². After prolonged Ar sputtering, this fluence dependence could be observed again and thus is not caused by insufficient sample cleaning.

Sputtering yields were obtained from this steady state for different angles of incidence, which are shown in Figure 1b. Experimental results (dots) for 1 keV (green), 2 keV (blue), and 5 keV (orange) are plotted over the angle of incidence in respect to the surface normal. The comparison to SDTrimSP (dashed lines) shows a consistently lower experimental sputtering yield than in the simulations. This difference represents a discrepancy to the findings for He⁺ and Ar⁺ on augite, where experimental yields were found to agree precisely with SDTrimSP (Biber et al., 2020). Instead, the differences between experiment and SDTrimSP

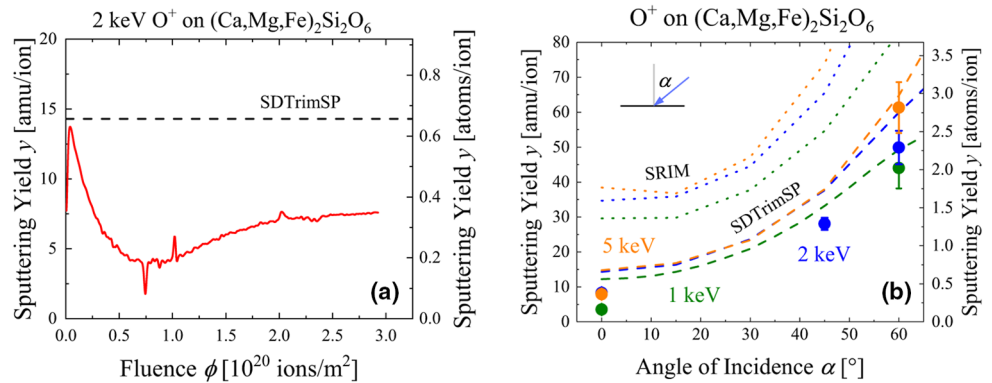


Figure 1. (a) An example of the measured fluence dependence of the sputtering yield of augite during continuous irradiation with 2 keV O⁺ under normal incidence. (b) The angular dependence of the sputtering yield in the steady state for 1 keV (green), 2 keV (blue), and 5 keV (orange) O⁺ ions. Experimental values (dots) are compared to simulations with SDTrimSP (static mode, dashed lines) and SRIM (Stopping and Range of Ions in Matter).

simulation are close to constant, as is shown in Table 3. Sputtering values simulated by SRIM (dotted lines) overestimate the yield by a factor of 2 and do not accurately represent the measured sputtering yields. This observation is in agreement with previous comparisons between SDTrimSP and SRIM for oxides, where the sputtering yields predicted by SRIM are too high (Schaible et al., 2017).

3.2. O⁺ Measurements on Wollastonite

To investigate a possible universal deviation for O⁺ ions between SDTrimSP and experiments, wollastonite (CaSiO₃) samples were irradiated with 2 and 5 keV O⁺ ions. For this purpose, QCMs from the same batches as in Szabo et al. (2020a) were irradiated (see Table 1 for results of the composition analysis). The resulting angular dependence is shown in Figure 2a. Experimental values for 2 keV (blue) and 5 keV (orange) are compared to SDTrimSP simulations (static mode, dashed lines) and SRIM simulations (dotted lines). Consistent with previous findings for wollastonite, SDTrimSP predicts the measured sputtering yields very well. SRIM calculations significantly overestimate the absolute values of the measured yields by a factor of about 2, as similarly observed for augite.

This good agreement of SDTrimSP simulations and experiments with wollastonite samples represents a discrepancy to the measurements with augite samples as it is shown in Figure 2b. The ratio between experimental and SDTrimSP-simulated sputtering yields are plotted for wollastonite in blue and augite in red. For He, O, and Ar projectiles, data for different angles and energies are used (including data taken from Szabo et al. [2018, 2020a] and Biber et al. [2020]). For wollastonite, all measurements show a generally good agreement with the calculation within the shaded area representing a $\pm 20\%$ difference. For augite, this holds for He and Ar, but measured O yields are systematically lower.

3.3. O₂⁺ Measurements

As reported by Nenon et al. (2019), the sputtering contribution by O₂⁺ ions at Phobos might even be higher than by atomic O ions. To investigate possible molecular effects, we therefore measured sputtering yields of augite under irradiation with O₂⁺ ions at normal incidence and under 60°. Figure 3 shows a comparison of the measured sputtering yields per O atom between atomic (blue) and molecular (red) ions at the same kinetic energy per O atom (i.e., for identical impact velocities). All experimental findings agree within their error bars and no significant deviations for molecular ions can be reported for the measured energies of 1 and 2 keV/O.

Table 3

Overview of the observed differences of the experimental sputtering yields compared to SDTrimSP simulations in the static mode for 1, 2, and 5 keV O⁺ on augite

	Observed difference (absolute) (amu/ion)
1 keV O ⁺	-8.54 ± 2.71
2 keV O ⁺	-6.46 ± 2.49
5 keV O ⁺	-6.70 ± 3.24

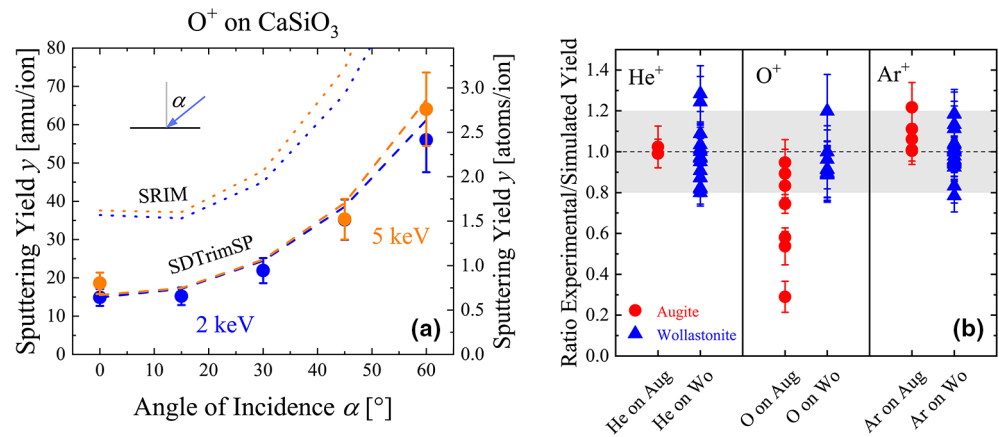


Figure 2. (a) The angular dependence of wollastonite sputtering yields under O irradiation. Experimental values (dots) for 2 keV (blue) and 5 keV (orange) are shown with results from SDTrimSP (static mode, dashed lines) and SRIM (dotted lines). (b) The ratio of experimental and simulated sputtering yields (from SDTrimSP) for augite (red) and wollastonite (blue). This figure includes data from Szabo et al. (2018, 2020a) and Biber et al. (2020). SRIM, Stopping and Range of Ions in Matter.

3.4. C⁺ and CO₂⁺ Measurements

To test for possible molecular effects of augite sputtering under CO₂ ion bombardment, sputtering by C⁺ and CO₂⁺ irradiation was performed. Augite sputtering yields for C⁺ are shown in Figure 4a. The experimental results for 2 keV (blue dots) and 5 keV (orange dots) behave similar to the O sputtering yields reported in Section 3.1. SDTrimSP (static mode, dashed lines) fits the experimental trend much better than SRIM (dotted lines). For normal incidence, experimental sputtering yields are lower than in the simulation. For 60°, the agreement is good, but the absolute error is also larger.

Results for 2 keV CO₂⁺ irradiations are presented in Figure 4b (dots) together with an SDTrimSP calculation (static mode, dashed line). To obtain the simulation, an immediate dissociation upon impact and subsequent independent collision cascades for the three atoms making up the CO₂ molecule were assumed. Thus, simulations for 545 eV C and two 727 eV O atoms, which make up 2 keV CO₂, were performed and the results were summed up. The comparison between experiment and calculation in Figure 4b shows that, in general, the absolute values are similar.

4. Discussion

4.1. Sputtering Behavior of Augite

The experimental sputtering yields of augite under O⁺ bombardment all show lower values than static simulations with SDTrimSP. They represent a notable difference compared to noble gas measurements and O⁺ irradiations on CaSiO₃, which can be consistently described by SDTrimSP with identical simulation parameters. This is emphasized in Figure 5a, where a comparison between measured and simulated sputtering yields for the irradiation of augite (red) and wollastonite (blue) with 2 keV O⁺ is presented. SDTrimSP predicts practically identical sputtering yields for the two materials as their differences in composition are small. As already shown in Figure 2, wollastonite results agree very well with SDTrimSP simulations, while experimental results from augite are consistently smaller.

Figure 5b shows a similar comparison for the irradiation of augite and wollastonite with 2 keV Ar⁺ ions (wollastonite data taken from Szabo et al. [2018]). SDTrimSP again calculates close to identical sputtering yields for both materials, which is well reflected in the experimental findings over the whole range of investigated angles of incidence.

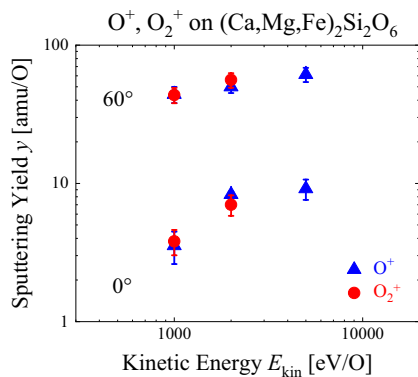


Figure 3. A comparison between measured sputtering yields under atomic (blue) and molecular (red) O ion irradiation for 0° and 60° incidences. Kinetic energy and sputtering yields are denoted per O atom to compare if a molecular ion can be treated as two independent atomic ions at the same velocity.

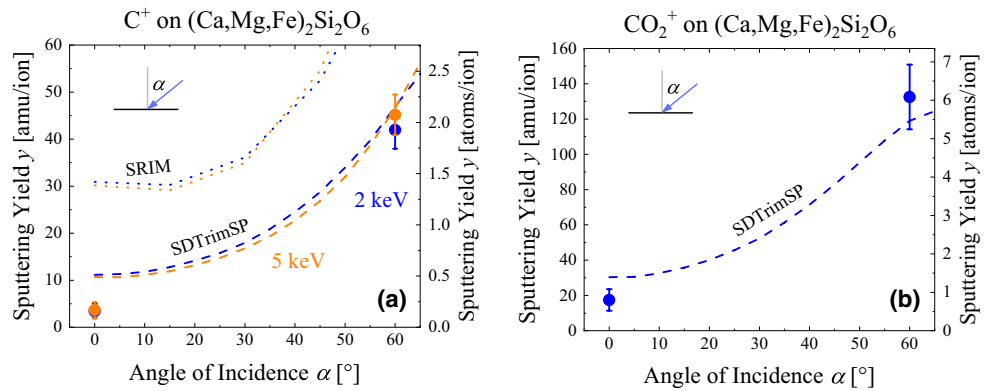


Figure 4. (a) Experimental sputtering yields (dots) for C^+ on augite are compared to SDTrimSP (static mode, dashed lines) and SRIM (dotted lines) for 2 keV (blue) and 5 keV (orange). (b) Results of measurements with 2 keV CO_2^+ ions (blue dots). The SDTrimSP curve (static mode, dashed blue line) is the sum of simulated sputtering yields under irradiation with atomic ions of the same velocity as 2 keV CO_2 . SRIM, Stopping and Range of Ions in Matter.

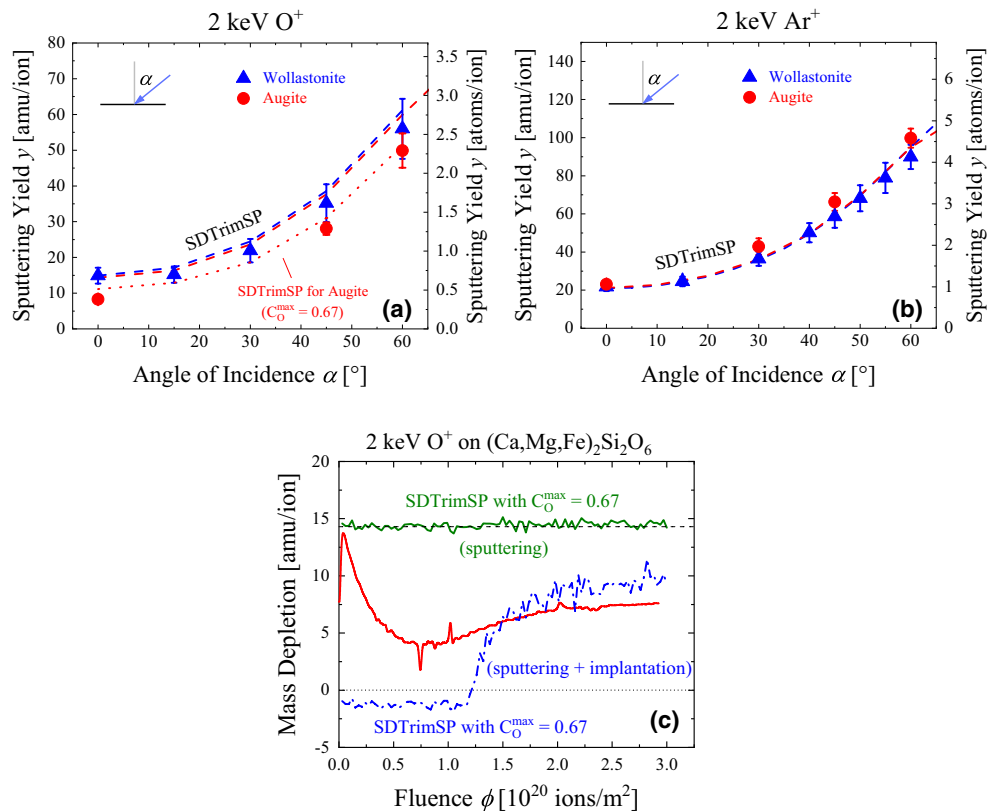


Figure 5. (a) Compilation for the measured sputtering yields under 2 keV O^+ bombardment for augite (red) and wollastonite (blue). Experimental values (dots) are compared to static SDTrimSP simulations (dashed lines). For augite, a calculation of the mass change from dynamic SDTrimSP simulations with an O concentration limit of 67% is included (red dotted line). (b) Comparison of the sputtering yields of augite and wollastonite from experiments and static SDTrimSP simulations for 2 keV Ar^+ (same symbols and colors as in Figure 5a). (c) Fluence-dependent mass depletion per ion for 2 keV O^+ . The experimental results (red) are compared to a SDTrimSP simulation with an O concentration limit of 67%. The simulated mass changes from sputtering and O implantation (blue dashed line) reproduce parts of the experimental behavior well. The mass changes from sputtering, with ignored implantation, remain constant (green line).

The differences in elemental composition between augite and wollastonite thus seem rather small to plausibly explain a different sputtering behavior. As a consequence, implantation of O ions is the more robust assumption as the QCM technique only allows the measurement of absolute mass changes. Then a superposition of a mass decrease due to sputtering and a mass increase due to implanted projectiles that stay bound in the sample would be observed for augite.

Implantation of O ions could also explain the observed fluence dependence of the measured mass changes as shown in Figure 1a. In the experiment, an initial sputtering yield decrease followed by an increase was measured. Figure 5c shows the same fluence dependence, but interpreted more generally as a mass depletion per ion. The experimental results are compared to an SDTrimSP simulation, where O implantation is included. In this simulation, the maximum local O concentration is limited to 0.67, which results in the simulated mass depletion per ion shown as the blue dashed line. The simulation strongly deviates at the beginning of the irradiation, where all stopped O ions are implanted. Here the mass decrease by sputtering and the mass increase by ion implantation are almost equivalent, even a net mass increase is calculated. However, when local saturation starts to occur (after a fluence of about 10^{20} ions/m²), the calculated mass change shows a similar tendency as observed in the experiment. The mass changes from sputtering alone are constant in the same simulation (green line), due to the low relative concentration changes at the sample surface. The observed mass change behavior is thus caused entirely by implantation of O projectiles.

Biber et al. (2020) performed similar simulations for the implantation of He ions into augite samples. They found that the steady-state fluence and the sputtering yields in the steady state agreed well with the measurement. However, in their experiments, the phase of net mass increase at low fluences was less extreme and changes to net sputtering are more continuous than in their SDTrimSP simulations. A similar behavior can be expected for the presented irradiation with O ions. Still, this cannot explain the fluence dependence in our experiment up to about 10^{20} ions/m², which indicates an increased sputtering.

In the steady state, a dynamic equilibrium forms where the same amount of O ions is sputtered as implanted. This results in slightly lower mass changes than when no implantation occurs, as is shown by the red dotted line in Figure 5a. Here the steady state results from dynamic simulations for 2 keV O⁺ irradiations under different angles of incidence for a fluence of 5×10^{20} O/m² are shown, leading to a better agreement for all measured values. In such dynamic simulations, the concentration changes are small and therefore the sputtering yields remain mostly constant (green line in Figure 5c). However, to reproduce the actual measured mass changes, implantation effects have to be considered.

Taking into account the results with CaSiO₃ samples, the presence of Ca, Si, and O in the sample alone does not seem to be responsible for the excess O⁺ ion implantation. Similar behavior should be expected for Mg as both Mg and Ca are alkaline earth metals. Future in situ composition analyses of planetary analog samples after O irradiation should be aimed for to get more insight into these effects.

Oxygen implantation by bonding to the Fe atoms in augite is thus a possible explanation for the observed lower mass changes. Nanophase Fe formation under solar wind ion bombardment has been found to coincide with a local reduction (Kuhlman et al., 2015; Loeffler et al., 2009), implantation of O ions could be connected to a reverse process. For example, the assumed O saturation concentration of 67% could roughly be attributed to the 9% Fe atoms in the augite target changing from FeO to Fe₂O₃. Some near-infrared spectral features of Phobos may be attributed to nanophase Fe that has formed as a result of the interaction with the solar wind (Fraeman et al., 2014); therefore, such effects could also be relevant for Phobos' surface. The Fe content of planetary regolith plays a special role for space weathering research, as the formation of nanophase Fe is seen as an important contribution to the reddened spectra of space-weathered surfaces (Hapke, 2001; Vernazza et al., 2009).

4.2. Sputtering Yields by Atomic and Molecular Ions From the Martian Atmosphere

Based on the measurements in Section 3.3, we conclude that the sputtering yields of O₂⁺ and two separate O⁺ ions are equivalent for the same kinetic energy per O atom within experimental uncertainty. Similarly, no significant molecular effects could be observed for the irradiation of augite with CO₂⁺ ions

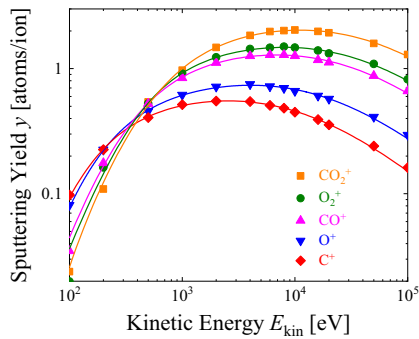


Figure 6. Sputtering yields under normal incidence for C^+ (red), O^+ (blue), CO^+ (magenta), O_2^+ (green), and CO_2^+ ions (orange). The dots show results from SDTrimSP simulations in the static mode and the lines denote a fit to these results using the Eckstein fitting formula. For the sputtering yields by molecular ions at specific energies, the sum of simulation results with individual atomic ions at the same velocity was taken.

(see Section 3.4). These findings agree with previous studies on the comparison between sputtering by atomic and molecular ions at kinetic energies in the keV range. Molecular sputtering effects have been reported for two energy regimes (Andersen & Bay, 1974, 1975; Dobes et al., 2011; Yao et al., 1998). For slow molecular ions with energies below about 1 keV/atom, it cannot be assumed that the molecule immediately dissociates upon impact. Higher momentum transfers than for atomic ions are possible, leading to increased sputtering yields, but only of about 25% (Dobes et al., 2011). For higher energies of several tens of keV, the collision cascades overlap and nonlinear effects can increase the sputtering yields. This high-energy effect should not play a significant role for Phobos as the ion fluxes in the Martian plasma environment at these high energies do not significantly contribute to the sputtering of its surface. Sputtering is instead dominated by ions below 10 keV, as it was calculated by Nenon et al. (2019).

Based on these observations and the reasonable agreement between experimental data and SDTrimSP simulations, sputtering yields for atmospheric ions impacting the surface of Phobos can be estimated. Figure 6 shows a compilation of SDTrimSP sputtering yield results from simulations in the static mode on an augite sample (dots) irradiated with C^+ (red), O^+ (blue), CO^+ (magenta), O_2^+ (green), and CO_2^+ (orange) under normal incidence at different energies. Molecular effects were disregarded for these simulations and the results for molecular ions were derived by summing up simulated yields for the respective atomic ions at the same impact velocity (i.e., the same specific energy E_{kin}/m). Figure 6 also includes fits to the simulation results with the fitting formula proposed by Eckstein and Preuss (2003), which describes the data very well (for more details on the fitting formula and tabulated fitting parameters, see the Appendix).

At the same kinetic energy, sputtering by molecular ions is mostly higher and the sputtering yield peak is shifted to higher energies. This is caused by the assumption that the molecular ion behaves the same as two atomic ions at the same velocity. For example, a 4 keV O_2^+ ion would be equivalent to two 2 keV O^+ ions and its sputtering yield is twice as high as for 2 keV O^+ . O_2^+ sputtering yields can then be up to a factor of 3 larger than O^+ yields at the same kinetic energy. Significant increases can also be observed for CO^+ and CO_2^+ ions. Nevertheless, Nenon et al. (2019) mention that MAVEN measurements of CO_2^+ ion fluxes were found to be significantly lower than those of O^+ and O_2^+ . In the context of these observations, the derived sputtering yields presented in Figure 6 suggest that it is a reasonable assumption to neglect sputtering by molecular ions apart from O_2^+ .

At the same kinetic energy, sputtering by molecular ions is mostly higher and the sputtering yield peak is shifted to higher energies. This is caused by the assumption that the molecular ion behaves the same as two atomic ions at the same velocity. For example, a 4 keV O_2^+ ion would be equivalent to two 2 keV O^+ ions and its sputtering yield is twice as high as for 2 keV O^+ . O_2^+ sputtering yields can then be up to a factor of 3 larger than O^+ yields at the same kinetic energy. Significant increases can also be observed for CO^+ and CO_2^+ ions. Nevertheless, Nenon et al. (2019) mention that MAVEN measurements of CO_2^+ ion fluxes were found to be significantly lower than those of O^+ and O_2^+ . In the context of these observations, the derived sputtering yields presented in Figure 6 suggest that it is a reasonable assumption to neglect sputtering by molecular ions apart from O_2^+ .

4.3. Consequences for Sputtering on Phobos

In the context of the space weathering of Phobos, the results from the presented sputtering experiments give a more accurate reflection of the erosion rates of Phobos' surface than previously assumed sputtering input data. Specifically, we want to investigate how these new results influence the role of sputtering by planetary O ions in the Martian tail region. Its contribution should be compared to the solar wind sputtering by H and He ions.

For the solar wind H^+ irradiation at 1 keV, we performed additional measurements with augite samples under normal incidence and found a precise agreement with SDTrimSP. Similar agreement has been found for He^+ at the solar wind energy of 4 keV by Biber et al. (2020). For planetary O ions, we also use SDTrimSP for calculating expected sputtering yields. As discussed in Section 4.1, we assume that the observed mass change discrepancies between experiment and SDTrimSP simulation are caused by projectile implantation. In order to calculate the sputtering effects on Phobos, SDTrimSP simulations were performed with the assumed Phobos composition shown in Table 1. Concentration changes due to O implantation are not taken into account, as SDTrimSP predicts them to be too small to cause significant changes in the sputtering yields (see Section 4.1). Following the above-presented experimental findings, the general

Table 4

A compilation of the calculated Phobos sputtering yields from the present study compared to the inputs used by Nenon et al. (2019), as well as the scaling factor, which is calculated from the ratio of the two datasets

	Sputtering yield derived from this work (atoms/ion)	Sputtering yield used by Nenon et al. (2019) (atoms/ion)	Scaling factor
1 keV H	0.015	<i>0.015</i>	1.0
4 keV He	0.092	<i>0.14</i>	0.657
SW, He/H 2.9%	0.01717	0.01852	0.927
16 keV O	0.642	<i>1.3</i>	0.494
Ratio 16 keV O sputtering yield/SW sputtering yield	37.4	70.2	0.533

Note. For the data used by Nenon et al. (2019), only the values in italics are stated explicitly in their publication. The remaining values were calculated following their description to allow a comparison with sputtering yields based on experimental data for augite.

Abbreviation: SW, solar wind.

assumptions by Nenon et al. (2019) to only take into account O^+ and O_2^+ ions and to disregard molecular effects are still valid.

Nenon et al. (2019) used sputtering inputs based on Ni sputtering yields published by Biersack and Eckstein (1984) for their calculation. Corresponding energy dependences are shown in Figure 1 in Poppe and Curry (2014). Concretely, they state following sputtering yields (see Table 3): 0.015 atoms/ion for 1 keV H (SDTrimSP with Phobos composition also gives 0.015 atoms/ion), 0.14 atoms/ion for 4 keV He (SDTrimSP: 0.092 atoms/ion), and 1.3 atoms/ion for 16 keV O (SDTrimSP: 0.64 atoms/ion). While the yield for H agrees precisely with our SDTrimSP simulation, our results indicate lower sputtering yields for He and O ions. Schaible et al. (2017) have also performed SDTrimSP simulations for the space weathering of SiO_2 and Al_2O_3 by H and He ions, reporting sputtering yields that are somewhat higher than ours. This can most probably be explained by the adapted input parameters we used to better describe our experimental findings (see Section 2.3 and Szabo et al. [2020a]).

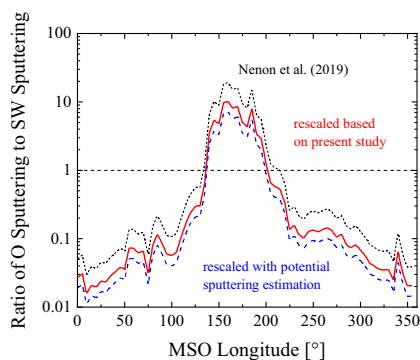


Figure 7. An evaluation of the ratio between O sputtering and solar wind sputtering based on the presented experimental findings. The black dashed line shows the results from Nenon et al. (2019) over different Mars-Solar-Orbital longitudes. The red line represents a rescaling based on the measured sputtering yields, and the blue dashed line gives the result of rescaling when a 43% increase of solar wind sputtering due to potential sputtering is considered (see Section 4.4). A reduction can be seen, but the conclusion is supported that sputtering by planetary O ions is by far the biggest contribution to space weathering on Phobos in the Martian downstream region.

With the solar wind composition from MAVEN measurements, a mean solar wind kinetic sputtering yield of 0.017 can be derived from the simulation values (He/H energy flux peak ratio of 2.9% [Nenon et al., 2019]). The yield inputs used by Nenon et al. (2019) result in a mean solar wind sputtering yield of 0.019. Therefore, their estimation of solar wind sputtering on Phobos agrees well with our calculation with a difference of about 10%. For O^+ sputtering, the energy dependence from Poppe and Curry (2014) can be well reproduced by rescaling the SDTrimSP simulations with a constant factor. However, the simulation results are by a factor of 2.02 smaller (−50.6%) than the O^+ sputtering yields assumed by Nenon et al. (2019). Table 4 gives an overview over the different sputtering yields.

Combining these inputs, the ratio of O sputtering and solar wind sputtering can be calculated. Based on the augite experiments, this ratio is by a factor of 1.88 lower (−46.7%) than the previously used values by Nenon et al. (2019). If this calculation is performed with the slightly different augite composition from TOF-ERDA instead of the assumed Phobos composition, it gives a reduction by a factor of 1.79 (−44.1%). This shows that the outcome is not sensitive to the exact element concentrations, which is important due to existing uncertainties about actual surface composition of Phobos.

The experimental results do not show a significant deviation from the previously estimated sputtering yield uncertainty of 2 (Nenon et al., 2019). The conclusion that planetary O ions can cause more sputtering on Phobos in the Martian tail region is thus not affected by our results. This is illustrated in Figure 7 where the ratio between the sputtering fluxes resulting from planetary O irradiation and solar wind irradiation is plotted over Mars-Solar-Orbital longitude. The result of the calculation from Nenon et al. (2019) shows a clear maximum in the Martian tail around longitudes of 180° (black dotted line). With a rescaling based on the presented experimental findings, the contribution by planetary O ions is still dominant in the tail by a factor of up to 10 and the longitudes where the ratio is above 1 are barely affected (red line). Averaged over a full Phobos orbit, the contribution from O sputtering to the total sputtering of Phobos' surface decreases from 22% to 13% compared to the calculation results by Nenon et al. (2019). This value was calculated for the whole surface of Phobos and does not take into account its tidal locking. The Mars-facing area of Phobos' surface will thus be much more affected by O sputtering from planetary ions.

4.4. Estimation of Potential Sputtering

Potential sputtering by multiply charged ions will not affect sputtering by Martian O ions on the surface of Phobos, but it will increase the solar wind sputtering by He^{2+} ions. Figure 7 includes a rescaling with an added estimation of the potential sputtering (blue dashed line). Szabo et al. (2020a) calculated a significant increase for the total solar wind sputtering of wollastonite due to potential sputtering. O atoms have been found to be preferentially sputtered by the potential energy of the ions (Sporn et al., 1997), which leads to a significant O depletion of the surface. The increase of the sputtering yield depends on the fluence. Based on the measurements of the potential sputtering by He^{2+} ions on wollastonite, the average sputtering yield of all solar wind ions was calculated to be a factor of about 2 higher for a fresh mineral surface than for only kinetic sputtering. The increase compared to only kinetic sputtering then reaches 1.43 in the steady state after prolonged ion bombardment, when normal incidence is considered (Szabo et al., 2020a). Similar sputtering yields are derived by Barghouty et al. (2011) for the lunar analog KREEP and by Hijazi et al. (2017) for anorthite. The fluence dependence of potential sputtering is caused by a decrease of the O content at the surface as the ions' potential energy only causes additional sputtering of O atoms. The calculation of potential sputtering on wollastonite predicts a decrease of the surface O concentration from 60% to about 30% due to solar wind sputtering (Szabo et al., 2020a). So far, no potential sputtering data exists for augite samples, but the differences in potential sputtering behavior between wollastonite and augite are expected to be small due to their similar composition.

The fluence needed to reach this steady state corresponds to several hundred years of solar wind irradiation. A steady state on the exposed surface can be assumed as recent calculations estimate the timescales for surface refreshing to be 10^3 – 10^6 years (Ballouz et al., 2019). An uncertainty for the total effect of multiply charged ions is introduced by the potential sputtering increase being constant for all investigated angles of incidence (Szabo et al., 2020a). The relative increase will be smaller under shallow angles of incidence, which is relevant for rough and porous surfaces (Cassidy & Johnson, 2005; Küstner et al., 1998). For the consideration of a realistic scenario, a more detailed treatment would be needed to quantify the effects of potential sputtering. Nevertheless, an increase of solar wind sputtering and a decrease of the O concentration at the surface can also be expected on Phobos due to the He^{2+} component of the solar wind.

The blue dashed line in Figure 7 shows a rescaling with a 43% increase of the total solar wind sputtering, as an approximation for the effects of potential sputtering. This increase of 43% corresponds to the calculated steady-state increase under normal incidence from Szabo et al. (2020a). The ratio of O sputtering and solar wind sputtering is again somewhat lower, but O sputtering still significantly dominates at longitudes around 180° . Averaged over the orbit of Phobos, O sputtering then contributes 10% to the total sputtering of the surface of Phobos.

The experimental data presented in this study support the results that atmospheric O ions are the dominating contribution to the sputtering of Phobos' surface in the Martian tail region, as previously calculated by Nenon et al. (2019) and Poppe and Curry (2014). This even holds when uncertainties in surface composition and potential sputtering effects are considered.

5. Summary and Conclusion

Sputtering experiments under O^+ , O_2^+ , C^+ , and CO_2^+ irradiation were performed with augite samples on a QCM as a laboratory analog for the surface of Phobos. Measured sputter yields by O^+ bombardment are consistently lower than SDTrimSP simulations that otherwise precisely agree with He and Ar sputtering yields. Experiments on wollastonite sputtered by O ions reveal that this behavior does not universally occur for mineral samples. Instead, it could be linked to O implantation, possibly through bonding to Fe atoms in the augite sample. Dynamic SDTrimSP simulations, which include O implantation until a local O concentration of 67% is reached, lead to a much improved agreement with the experimental values. Further investigation and quantification of the amount of implanted O ions should be a goal for future analysis. In situ methods that would allow distinguishing between the original O content of the sample and the implanted O atoms could give important insights into the modification of planetary surfaces.

The possibility of increased sputtering yields due to molecular effects was investigated for O_2 and CO_2 ions. In accordance with previous publications, no evidence was found for such effects in the low keV range, which has the biggest contribution to sputtering on the surface of Phobos. Previous assumptions that treated O_2 ions as equivalent to two atomic ions at the same velocity could thus be validated. Some additional molecular effects might occur at lower energies, but they are expected to be small. Additionally, CO_2 ions can be assumed to only play a small role in sputtering of Phobos' surface as O_2^+ and O^+ ion fluxes from the upper Martian atmosphere layers represent the dominant contributions to ion precipitation on Phobos. Should the need arise to take more atmospheric species into account, sputtering yields based on SDTrimSP simulations are given in Figure 6 for several atomic and molecular ions over a broad energy range. These sputter yields are of superior accuracy compared to simple SRIM simulations with no experimental reference. SRIM calculations can be off by a factor of more than 2 as our experiments have shown. The values shown in Figure 6 should be well suited to calculate the sputtering of materials similar to the assumed Phobos composition. For larger deviations in elemental concentrations, SDTrimSP simulations with the respective surface composition will give better results.

For the general assessment of space weathering on Phobos, sputtering yields by atmospheric O ions as well as by solar wind ions were compared based on the new, more precise experimental input data. The measured sputtering yields suggest that O ions are less dominant for sputtering on Phobos than assumed in previous modeling efforts by Poppe and Curry (2014) as well as (Nenon et al., 2019), but their qualitative results are not affected by this rescaling. Our experiments support the concept that atmospheric O ions are the most important cause of sputtering on Phobos in the Martian tail region. This underlines the unique space weathering scenario on Phobos, which is alternately sputtered by the solar wind and by atmospheric ions. In total, solar wind ions are still dominant for sputtering. Our calculations suggest that atmospheric O ions contribute between about 10% and 15% to the total sputtering of Phobos' surface averaged over one orbit. Due to the tidal locking of Phobos, the sputtering by O ions will be dominant on its Mars-facing hemisphere.

The results of this study also emphasize the importance of sputtering experiments with planetary analogs to provide accurate sputtering yield inputs. Relying on simulated values without previous knowledge on the relevant system or using sputtering yields from completely different samples will result in additional uncertainties. As modeling approaches are becoming more sophisticated and accurate, the requirements for sputtering inputs will also increase. Additionally, effects that are not included in the present simulations should be investigated such as potential sputtering or ion implantation. This also holds for future research about Phobos. The role of potential sputtering on Phobos should be investigated more precisely concerning its fluence dependence and sputtering of rough surfaces. It should especially be evaluated if the increased O flux on Phobos affects the fluence dependence of potential sputtering in an interplay with the solar wind H^+ and He^{2+} .

Concerning implantation effects, implanted solar wind H could play a role in formation of Fe-bearing nanophases on Phobos (Fraeman et al., 2014). For remote observation of Phobos and similar bodies, it would be important to determine if this is relevant. Biber et al. (2020) also found He implantation of up to 10 at% at room temperature in the same pyroxene samples as used in the present study. The observed

temperature of 530 K that is necessary for He removal, which has also been similarly determined for other minerals (Lord, 1968), will not be reached on Phobos (Lynch et al., 2007). Therefore, the surface regolith of Phobos could have a higher He content than expected for Moon or Mercury. Solar wind ion implantation is also of importance for the second Martian moon Deimos. It is significantly further away from Mars than Phobos, and space weathering will be dominated by the solar wind. It thus remains an important goal that more information about the chemical and mineralogical composition of Phobos and Deimos becomes available and to further analyze such effects. This would allow for a better understanding of their space weathering and hence a better understanding of the development of the Martian moons.

Appendix

Eckstein and Preuss (2003) propose the following fitting formula for the energy dependence of the sputtering yield with fitting parameters q , λ , μ and E_{th} :

$$Y(E_0) = q s_n^{KrC}(\epsilon) \frac{\left(\frac{E_0}{E_{th}} - 1\right)^\mu}{\lambda + \left(\frac{E_0}{E_{th}} - 1\right)^\mu}$$

Here E_0 describes the ion's kinetic energy and $s_n^{KrC}(\epsilon)$ denotes the nuclear stopping power from the KrC potential:

$$s_n^{KrC}(\epsilon) = \frac{0.5 \ln(1 + 1.2288\epsilon)}{\epsilon + 0.1728\sqrt{\epsilon} + 0.008\epsilon^{0.1504}}$$

In this scope, the reduced energy

$$\epsilon = E_0 \frac{M_2}{M_1 + M_2} \frac{a_L}{Z_1 Z_2 e^2}$$

as well as the Lindhard screening length a_L are defined for an atomic ion hitting a mono-elemental target with atomic numbers Z_1 , Z_2 , and atomic masses M_1 , M_2 . This differs from the presented case, where atomic and molecular ions sputter a composite target.

For this purpose, we use the following expression for the reduced energy and introduce a fifth fitting parameter ϵ_L following the notation by Eckstein and Preuss (2003):

$$\epsilon = E_0 \epsilon_L$$

This formula was applied to individually fit the energy dependence of the SDTrimSP simulated sputtering yields by bombardment with C^+ , O^+ , CO^+ , O_2^+ , and CO_2^+ ions. The results are shown as the full lines in Figure 6 in Section 4.2 and describe the simulated sputtering yields very well over the whole energy range. Table A1 gives an overview of the obtained values for the fitting parameters.

Table A1

Results for the Fitting Parameters that Describe the Energy Dependence of the Sputtering Yield Under Irradiation with C^+ , O^+ , CO^+ , O_2^+ , and CO_2^+ Ions at Normal Incidence

	Q	λ	μ	E_{th}	ϵ_L
C^+	1.43484	13.4059	1.45022	22.7426	1.26802×10^{-4}
O^+	1.89964	20.3068	1.50222	22.882	7.55614×10^{-5}
CO^+	3.32419	69.2758	1.5104	21.2016	4.57931×10^{-5}
O_2^+	3.81371	335.877	1.64781	12.0068	3.7848×10^{-5}
CO_2^+	5.27316	41.0917	1.4027	39.2853	2.89859×10^{-5}

Data Availability Statement

The data presented in this manuscript is available at Figshare (Szabo et al., 2020b). The computational results presented have been achieved using the Vienna Scientific Cluster (VSC). The authors are grateful to Michael Schmid (Institute of Applied Physics, TU Wien) for his continued support with the QCM electronics.

Acknowledgments

Financial support has been provided by the Austrian Science Fund FWF (Project No. I 4101-N36) and by KKKÖ (Commission for the Coordination of Fusion research in Austria at the Austrian Academy of Sciences - ÖAW) as well as the Swiss National Science Foundation Fund (200021L_182771/1). Support by VR-RFI (contract #2017-00646_9) and the Swedish Foundation for Strategic Research (SSF, contract RIF14-0053) supporting operation of the accelerator at Uppsala University is gratefully acknowledged.

References

Andersen, H., & Bay, H. (1974). Nonlinear effects in heavy-ion sputtering. *Journal of Applied Physics*, *45*(2), 953–954. <https://doi.org/10.1063/1.1663348>

Andersen, H., & Bay, H. L. (1975). Heavy-ion sputtering yields of gold: Further evidence of nonlinear effects. *Journal of Applied Physics*, *46*(6), 2416–2422. <https://doi.org/10.1063/1.321910>

Aumayr, F., & Winter, H. (2004). Potential sputtering. *Philosophical Transactions of the Royal Society of London A: Mathematical, Physical and Engineering Sciences*, *362*(1814), 77–102. <https://doi.org/10.1098/rsta.2003.1300>

Ballouz, R.-L., Baresi, N., Crites, S. T., Kawakatsu, Y., & Fujimoto, M. (2019). Surface refreshing of Martian moon Phobos by orbital eccentricity-driven grain motion. *Nature Geoscience*, *12*(4), 229–234. <https://doi.org/10.1038/s41561-019-0323-9>

Barabash, S., Fedorov, A., Lundin, R., & Sauvaud, J.-A. (2007). Martian atmospheric erosion rates. *Science*, *315*(5811), 501–503. <https://doi.org/10.1126/science.1134358>

Barghouty, A. F., Meyer, F. W., Harris, P. R., & Adams, J. H. (2011). Solar-wind protons and heavy ions sputtering of lunar surface materials. *Nuclear Instruments and Methods in Physics Research Section B: Beam Interactions with Materials and Atoms*, *269*(11), 1310–1315. <https://doi.org/10.1016/j.nimb.2010.12.033>

Berger, B. M., Szabo, P. S., Stadlmayr, R., & Aumayr, F. (2017). Sputtering measurements using a quartz crystal microbalance as a catcher. *Nuclear Instruments and Methods in Physics Research Section B: Beam Interactions with Materials and Atoms*, *406*, 533–537. <https://doi.org/10.1016/j.nimb.2016.11.039>

Biber, H., Szabo, P. S., Jäggi, N., Wallner, M., Stadlmayr, R., Moro, M. V., et al. (2020). Solar wind Helium ion interaction with Mg and Fe rich pyroxene as Mercury surface analogue. *Nuclear Instruments and Methods in Physics Research Section B: Beam Interactions with Materials and Atoms*, *480*, 10–15. <https://doi.org/10.1016/j.nimb.2020.07.021>

Biersack, J., & Eckstein, W. (1984). Sputtering studies with the Monte Carlo program TRIM. *SP Applied Physics A*, *34*(2), 73–94. <https://doi.org/10.1007/BF00614759>

Carlsson, E., Fedorov, A., Barabash, S., Budnik, E., Grigoriev, A., Gunell, H., et al. (2006). Mass composition of the escaping plasma at Mars. *Icarus*, *182*(2), 320–328. <https://doi.org/10.1016/j.icarus.2005.09.020>

Carrez, P., Demyk, K., Cordier, P., Gengembre, L., Grimblot, J., D'Hendecourt, L., et al. (2002). Low-energy helium ion irradiation-induced amorphization and chemical changes in olivine: Insights for silicate dust evolution in the interstellar medium. *Meteoritics & Planetary Science*, *37*(11), 1599–1614. <https://doi.org/10.1111/j.1945-5100.2002.tb00814.x>

Cassidy, T. A., & Johnson, R. E. (2005). Monte Carlo model of sputtering and other ejection processes within a regolith. *Icarus*, *176*(2), 499–507. <https://doi.org/10.1016/j.icarus.2005.02.013>

Cipriani, F., Witasse, O., Leblanc, F., Modolo, R., & Johnson, R. E. (2011). A model of interaction of Phobos' surface with the Martian environment. *Icarus*, *212*(2), 643–648. <https://doi.org/10.1016/j.icarus.2011.01.036>

Deighan, J., Chaffin, M., Chaufray, J. Y., Stewart, A. I. F., Schneider, N., Jain, S. K., et al. (2015). MAVEN IUVS observation of the hot oxygen corona at Mars. *Geophysical Research Letters*, *42*, 9009–9014. <https://doi.org/10.1002/2015GL065487>

Dobes, K., Naderer, P., Lachaud, N., Eisenmenger-Sittner, C., & Aumayr, F. (2011). Sputtering of tungsten by N+ and N2+ ions: Investigations of molecular effects. *Physica Scripta*, *T145*, 014017. <https://doi.org/10.1088/0031-8949/2011/T145/014017>

Dubinin, E., Lundin, R., Norberg, O., & Pissarenko, N. (1993). Ion acceleration in the Martian tail: Phobos observations. *Journal of Geophysical Research*, *98*(A3), 3991–3997. <https://doi.org/10.1029/92JA02233>

Dubinin, E., Winningham, D., Fränz, M., Woch, J., Lundin, R., Barabash, S., et al. (2006). Solar wind plasma protrusion into the Martian magnetosphere: ASPERA-3 observations. *Icarus*, *182*(2), 343–349. <https://doi.org/10.1016/j.icarus.2005.08.023>

Eckstein, W., & Preuss, R. (2003). New fit formulae for the sputtering yield. *Journal of Nuclear Materials*, *320*(3), 209–213. [https://doi.org/10.1016/S0022-3115\(03\)00192-2](https://doi.org/10.1016/S0022-3115(03)00192-2)

Fraeman, A., Murchie, S., Arvidson, R., Clark, R., Morris, R., Rivkin, A., & Vilas, F. (2014). Spectral absorptions on Phobos and Deimos in the visible/near infrared wavelengths and their compositional constraints. *Icarus*, *229*, 196–205. <https://doi.org/10.1016/j.icarus.2013.11.021>

Galli, A., Vorburger, A., Wurz, P., Cerubini, R., & Tulej, M. (2018a). First experimental data of sulphur ions sputtering water ice. *Icarus*, *312*, 1–6. <https://doi.org/10.1016/j.icarus.2018.04.029>

Galli, A., Vorburger, A., Wurz, P., Pommerol, A., Cerubini, R., Jost, B., et al. (2018b). 0.2 to 10 keV electrons interacting with water ice: Radiolysis, sputtering, and sublimation. *Planetary and Space Science*, *155*, 91–98. <https://doi.org/10.1016/j.pss.2017.11.016>

Galli, A., Vorburger, A., Wurz, P., & Tulej, M. (2017). Sputtering of water ice films: A re-assessment with singly and doubly charged oxygen and argon ions, molecular oxygen, and electrons. *Icarus*, *291*, 36–45. <https://doi.org/10.1016/j.icarus.2017.03.018>

Galutschek, E., Trassl, R., Salzborn, E., Aumayr, F., & Winter, H. P. (2007). Compact 14.5 GHz all-permanent magnet ECRIS for experiments with slow multicharged ions. *Journal of Physics: Conference Series*, *58*(1), 395. <https://doi.org/10.1088/1742-6596/58/1/090>

Hapke, B. (2001). Space weathering from Mercury to the asteroid belt. *Journal of Geophysical Research*, *106*(E5), 10039–10073. <https://doi.org/10.1029/2000JE001338>

Hayderer, G., Schmid, M., Varga, P., Winter, H. P., & Aumayr, F. (1999). A highly sensitive quartz-crystal microbalance for sputtering investigations in slow ion-surface collisions. *Review of Scientific Instruments*, *70*(9), 3696. <https://doi.org/10.1063/1.1149979>

Hijazi, H., Bannister, M. E., Meyer, H. M., Rouleau, C. M., Barghouty, A. F., Rickman, D. L., & Meyer, F. W. (2014). Anorthite sputtering by H+ and Ar3+ (q = 1–9) at solar wind velocities. *Journal of Geophysical Research: Space Physics*, *119*, 8006–8016. <https://doi.org/10.1002/2014JA020140>

Hijazi, H., Bannister, M., Meyer, H., Rouleau, C. M., & Meyer, F. (2017). Kinetic and potential sputtering of an anorthite-like glassy thin film. *Journal of Geophysical Research: Planets*, *122*, 1597–1609. <https://doi.org/10.1002/2017JE005300>

Hofäss, H., Zhang, K., & Mutzke, A. (2014). Simulation of ion beam sputtering with SDTrimSP, TRIDYN and SRIM. *Applied Surface Science*, *310*, 134–141. <https://doi.org/10.1016/j.apsusc.2014.03.152>

Hurley, D. M., Cook, J. C., Retherford, K. D., Greathouse, T., Gladstone, G. R., Mandt, K., et al. (2017). Contributions of solar wind and micrometeoroids to molecular hydrogen in the lunar exosphere. *Icarus*, *283*, 31–37. <https://doi.org/10.1016/j.icarus.2016.04.019>

Jakosky, B. M., Lin, R., Grebowsky, J., Luhmann, J., Mitchell, D., Beutelschies, G., et al. (2015). The Mars atmosphere and volatile evolution (MAVEN) mission. *Space Science Reviews*, *195*(1–4), 3–48. <https://doi.org/10.1007/s11214-015-0139-x>

Kuhlman, K. R., Sridharan, K., & Kvit, A. (2015). Simulation of solar wind space weathering in orthopyroxene. *Planetary and Space Science*, *115*, 110–114. <https://doi.org/10.1016/j.pss.2015.04.003>

- Küstner, M., Eckstein, W., Dose, V., & Roth, J. (1998). The influence of surface roughness on the angular dependence of the sputter yield. *Nuclear Instruments and Methods in Physics Research Section B: Beam Interactions with Materials and Atoms*, 145(3), 320–331. [https://doi.org/10.1016/S0168-583X\(98\)00399-1](https://doi.org/10.1016/S0168-583X(98)00399-1)
- Leblanc, F., & Johnson, R. E. (2010). Mercury exosphere I. Global circulation model of its sodium component. *Icarus*, 209(2), 280–300. <https://doi.org/10.1016/j.icarus.2010.04.020>
- Li, G. Z., Matlock, T. S., Goebel, D. M., Dodson, C. A., Matthes, C. S., Ghoniem, N. M., & Wirz, R. E. (2017). In situ plasma sputtering and angular distribution measurements for structured molybdenum surfaces. *Plasma Sources Science and Technology*, 26(6), 065002. <https://doi.org/10.1088/1361-6595/aa6a7d>
- Loeffler, M. J., Dukes, C. A., & Baragiola, R. A. (2009). Irradiation of olivine by 4 keV He⁺: Simulation of space weathering by the solar wind. *Journal of Geophysical Research*, 114(E03003). <https://doi.org/10.1029/2008JE003249>
- Lord, H. (1968). Hydrogen and helium ion implantation into olivine and enstatite: Retention coefficients, saturation concentrations, and temperature-release profiles. *Journal of Geophysical Research*, 73(16), 5271–5280. <https://doi.org/10.1029/JB073i016p05271>
- Lynch, D. K., Russell, R. W., Rudy, R. J., Mazuk, S., Venturini, C. C., Hammel, H., et al. (2007). Infrared Spectra of Deimos (1–13 μm) and Phobos (3–13 μm). *The Astronomical Journal*, 134(4), 1459. <https://doi.org/10.1086/519975>
- Mahaffy, P. R., Benna, M., Elrod, M., Yelle, R. V., Bougher, S. W., Stone, S. W., & Jakosky, B. M. (2015). Structure and composition of the neutral upper atmosphere of Mars from the MAVEN NGIMS investigation. *Geophysical Research Letters*, 42, 8951–8957. <https://doi.org/10.1002/2015GL065329>
- Mahaffy, P. R., Webster, C. R., Atreya, S. K., Franz, H., Wong, M., Conrad, P. G., et al. (2013). Abundance and isotopic composition of gases in the Martian atmosphere from the Curiosity rover. *Science*, 341(6143), 263–266. <https://doi.org/10.1126/science.1237966>
- Marchi, S., Brunetto, R., Magrin, S., Lazzarin, M., & Gandolfi, D. (2005). Space weathering of near-earth and main belt silicate-rich asteroids: Observations and ion irradiation experiments. *Astronomy & Astrophysics*, 443(3), 769–775. <https://doi.org/10.1051/0004-6361:20053525>
- Moro, M. V., Holeňák, R., Medina, L. Z., Jansson, U., & Primetzhofer, D. (2019). Accurate high-resolution depth profiling of magnetron sputtered transition metal alloy films containing light species: A multi-method approach. *Thin Solid Films*, 686, 137416. <https://doi.org/10.1016/j.tsf.2019.137416>
- Mutzke, A., Schneider, R., Eckstein, W., Dohmen, R., Schmid, K., Toussaint, U. V., & Badelow, G. (2019). *SDTrimSP Version 6.00: IPP Report*, Garching, Germany: Max-Planck-Institut für Plasmaphysik.
- Nenon, Q., Poppe, A. R., Rahmati, A., Lee, C. O., McFadden, J. P., & Fowler, C. M. (2019). Phobos surface sputtering as inferred from MAVEN ion observations. *Journal of Geophysical Research: Planets*, 124, 3385–3401. <https://doi.org/10.1029/2019JE006197>
- Pfleger, M., Lichtenegger, H. I. M., Wurz, P., Lammer, H., Kallio, E., Alho, M., et al. (2015). 3D-modeling of Mercury's solar wind sputtered surface-exosphere environment. *Planetary and Space Science*, 115, 90–101. <https://doi.org/10.1016/j.pss.2015.04.016>
- Plainaki, C., Milillo, A., Mura, A., Orsini, S., Massetti, S., & Cassidy, T. (2012). The role of sputtering and radiolysis in the generation of Europa exosphere. *Icarus*, 218(2), 956–966. <https://doi.org/10.1016/j.icarus.2012.01.023>
- Poppe, A., & Curry, S. (2014). Martian planetary heavy ion sputtering of Phobos. *Geophysical Research Letters*, 41, 6335–6341. <https://doi.org/10.1002/2014GL061100>
- Poppe, A., Curry, S., & Fatemi, S. (2016). The Phobos neutral and ionized torus. *Journal of Geophysical Research: Planets*, 121, 770–783. <https://doi.org/10.1002/2015JE004948>
- Ramstad, R., Barabash, S., Futaana, Y., Nilsson, H., & Holmström, M. (2017). Global Mars-solar wind coupling and ion escape. *Journal of Geophysical Research: Space Physics*, 122, 8051–8062. <https://doi.org/10.1002/2017JA024306>
- Ramstad, R., Barabash, S., Futaana, Y., Nilsson, H., & Holmström, M. (2018). Ion escape from Mars through time: An extrapolation of atmospheric loss based on 10 years of Mars express measurements. *Journal of Geophysical Research: Planets*, 123, 3051–3060. <https://doi.org/10.1029/2018JE005727>
- Rivkin, A., Brown, R. H., Trilling, D. E., Bell, J., III, & Plassmann, J. (2002). Near-infrared spectrophotometry of Phobos and Deimos. *Icarus*, 156(1), 64–75. <https://doi.org/10.1006/icar.2001.6767>
- Russell, C. T., Luhmann, J. G., & Strangeway, R. J. (2016). *Space Physics: An introduction*. Cambridge University Press.
- Sauerbrey, G. (1959). Verwendung von Schwingquarzen zur Wägung dünner Schichten und zur Mikrowägung. *Zeitschrift für Physik*, 155(2), 206–222. <https://doi.org/10.1007/BF01337937>
- Schaible, M., Dukes, C., Hutcherson, A., Lee, P., Collier, M., & Johnson, R. (2017). Solar wind sputtering rates of small bodies and ion mass spectrometry detection of secondary ions. *Journal of Geophysical Research: Planets*, 122, 1968–1983. <https://doi.org/10.1002/2017JE005359>
- Schmitz, J., Mutzke, A., Litnovsky, A., Klein, F., Tan, X., Wegener, T., et al. (2019). Preferential sputtering induced Cr-Diffusion during plasma exposure of WCrY smart alloys. *Journal of Nuclear Materials*, 526, 151767. <https://doi.org/10.1016/j.jnucmat.2019.151767>
- Sigmund, P. (1969). Theory of Sputtering. I. Sputtering yield of amorphous and polycrystalline targets. *Physical Review*, 184(2), 383–416. <https://doi.org/10.1103/PhysRev.184.383>
- Sporn, M., Libiseller, G., Neidhart, T., Schmid, M., Aumayr, F., Winter, H. P., et al. (1997). Potential sputtering of clean SiO₂ by slow highly charged ions. *Physical Review Letters*, 79(5), 945–948. <https://doi.org/10.1103/PhysRevLett.79.945>
- Stadlmayr, R., Szabo, P., Mayer, D., Cupak, C., Dittmar, T., Bischoff, L., et al. (2020). Sputtering of nanostructured tungsten and comparison to modelling with TRIDYN. *Journal of Nuclear Materials*, 532, 152019. <https://doi.org/10.1016/j.jnucmat.2020.152019>
- Szabo, P. S., Biber, H., Jäggi, N., Brenner, M., Weichselbaum, D., Niggas, A., et al. (2020a). Dynamic potential sputtering of lunar analog material by solar wind ions. *The Astrophysical Journal*, 891(1), 100. <https://doi.org/10.3847/1538-4357/ab7008>
- Szabo, P. S., Biber, H., Jäggi, N., Wapfl, M., Stadlmayr, R., Primetzhofer, D., et al. (2020b). Experimental insights into space weathering of Phobos: Laboratory investigation of sputtering by atomic and molecular planetary ions [dataset]. <https://doi.org/10.6084/m9.figshare.12501179>
- Szabo, P. S., Chiba, R., Biber, H., Stadlmayr, R., Berger, B. M., Mayer, D., et al. (2018). Solar wind sputtering of wollastonite as a lunar analogue material—comparisons between experiments and Simulation. *Icarus*, 314, 98–105. <https://doi.org/10.1016/j.icarus.2018.05.028>
- Verigin, M., Shutte, N., Galeev, A., Gringauz, K., Kotova, G., Remizov, A., et al. (1991). Ions of planetary origin in the Martian magnetosphere (Phobos 2/TAUS experiment). *Planetary and Space Science*, 39(1–2), 131–137. [https://doi.org/10.1016/0032-0633\(91\)90135-W](https://doi.org/10.1016/0032-0633(91)90135-W)
- Vernazza, P., Binzel, R., Rossi, A., Fulchignoni, M., & Birlan, M. (2009). Solar wind as the origin of rapid reddening of asteroid surfaces. *Nature*, 458(7241), 993–995. <https://doi.org/10.1038/nature07956>
- Vernazza, P., Cipriani, F., Dukes, C., Fulvio, D., Howard, K., Witasse, O., et al. (2010). Meteorite analogs for Phobos and Deimos: Unraveling the origin of the Martian moons. *Meteoritics and Planetary Science Supplement*, 73, 5076.
- Vorburger, A., & Wurz, P. (2018). Europa's ice-related atmosphere: The sputter contribution. *Icarus*, 311, 135–145. <https://doi.org/10.1016/j.icarus.2018.03.022>

- Wurz, P., & Lammer, H. (2003). Monte-Carlo simulation of Mercury's exosphere. *Icarus*, *164*(1), 1–13. [https://doi.org/10.1016/S0019-1035\(03\)00123-4](https://doi.org/10.1016/S0019-1035(03)00123-4)
- Wurz, P., Rohner, U., Whitby, J. A., Kolb, C., Lammer, H., Dobnikar, P., & Martín-Fernández, J. A. (2007). The lunar exosphere: The sputtering contribution. *Icarus*, *191*(2), 486–496. <https://doi.org/10.1016/j.icarus.2007.04.034>
- Yao, Y., Hargitai, Z., Albert, M., Albridge, R., Barnes, A., Gilligan, J., et al. (1998). New molecular collisional interaction effect in low-energy sputtering. *Physical Review Letters*, *81*(3), 550. <https://doi.org/10.1103/PhysRevLett.81.550>
- Ziegler, J. F., Ziegler, M. D., & Biersack, J. P. (2010). SRIM – The stopping and range of ions in matter (2010). *Nuclear Instruments and Methods in Physics Research Section B: Beam Interactions with Materials and Atoms*, *268*(11), 1818–1823. <https://doi.org/10.1016/j.nimb.2010.02.091>